TITLE

Genetic insights into foveal morphology and its associations with pigmentation and age-related macular degeneration

AUTHOR LIST & AFFILIATIONS

David J. Green[1], Thomas H. Julian[1,2-4], David Romero-Bascones[5], Sofia Torchia[4], Heer N.V. Joisher[6-8], UK Biobank Eye and Vision Consortium, Unai Ayala[5], Maitane Barrenechea[5], Jay E. Self[9,10], Graeme C. Black[1,11], Tomas Fitzgerald[4], Ewan Birney[4], Constance L. Cepko[6-8], Joseph Carroll[12], Panagiotis I. Sergouniotis[1,2,4,11]

[1] Division of Evolution, Infection and Genomics, School of Biological Sciences, Faculty of Biology, Medicine and Health, University of Manchester, Manchester, UK.

[2] Manchester Royal Eye Hospital, Manchester University NHS Foundation Trust, Manchester, UK.

[3] Christabel Pankhurst Institute, The University of Manchester, Manchester, UK

[4] European Molecular Biology Laboratory, European Bioinformatics Institute (EMBL-EBI), Wellcome Genome Campus, Cambridge, UK

[5] Biomedical Engineering Department, Faculty of Engineering (MU-ENG), Mondragon Unibertsitatea, Mondragón, Spain.

[6] Department of Genetics, Blavatnik Institute, Boston, MA, USA

[7] Department of Ophthalmology, Harvard Medical School, Boston, MA, USA

[8] Howard Hughes Medical Institute, Chevy Chase, MD, USA

[9] Clinical and Experimental Sciences, Faculty of Medicine, University of Southampton, Southampton, UK

[10] Southampton Eye Unit, University Hospital Southampton NHS Foundation Trust, Southampton, UK

[11] Manchester Centre for Genomic Medicine, Saint Mary's Hospital, Manchester University NHS Foundation Trust, Manchester, UK

[12] Ophthalmology and Visual Sciences, Medical College of Wisconsin, Milwaukee, WI, USA

Correspondence to Panagiotis I. Sergouniotis (panagiotis.sergouniotis@manchester.ac.uk).

ABSTRACT

The fovea is the small depression at the neurosensory retina that underlies high-resolution central vision. It is vulnerable to disease and disruption of its architecture causes visual disability. Foveal morphology varies significantly across individuals. The molecular causes and functional consequences of this anatomical diversity are incompletely understood. Here, we extracted six foveal morphological parameters from Optical Coherence Tomography (OCT) images of 39,521 UK Biobank participants. We found notable variability in foveal morphology and detected significant links with sex and genetic ancestry. Genome-wide association studies identified 161 lead loci across the six foveal morphological parameters, implicating genes involved in pigmentation (e.g., *TYR*, *TSPAN10, GPR143*) and patterning (e.g., *FGFR2*, *PTPRD, CYP1A1*). Heritability estimates ranged from 29-43%. Foveal pit volume was associated with future risk of age-related macular degeneration (HR=1.1, p=0.0004), a finding supported by Mendelian randomization. These results establish foveal morphology as a highly heritable trait with notable influence over retinal disease risk.

INTRODUCTION

The fovea is a specialized structure at the centre of the retina. It has a key role in high-acuity vision, supports most daily life activities, and enables tasks such as reading and face recognition.[1,2] The fovea is affected in a range of retinal disorders, including common adult-onset diseases such as age-related macular degeneration (AMD) (which is associated with loss of foveal cells) and paediatric conditions like albinism (which is characterized by foveal hypoplasia).[2]

The fovea has been studied for more than a century. Despite this, there are significant gaps in our knowledge, including the extent to which the morphology of the foveal pit contributes to high-acuity vision; this is partly because animal models that are routinely used in research (e.g. most murine and teleost models) lack this morphological specialization.[2] Recent advances in genomics, data science and *in vivo* imaging technologies have transformed our ability to study complex biological structures like the fovea.[3] Another major enabler has been the increasing availability of large-scale cohorts with a rich phenotypic scope. One example is the UK Biobank, a biomedical resource containing in-depth genetic and health information from >500,000 individuals.[4] Many UK Biobank participants underwent enhanced phenotyping including visual function assessment (>130,000 volunteers) and imaging of the central retina (>84,000 volunteers);[5] the latter was obtained using optical coherence tomography (OCT), a non-invasive imaging modality that rapidly generates cross-sectional retinal scans at micrometre-resolution.[6]

The most prominent morphological feature of the human fovea is the pit, corresponding to a central excavation of the inner retinal layers. Previous imaging studies have highlighted substantial morphological variability in respect to the depth, width and volume of the pit.[1,7–12] This anatomical diversity is thought to arise from variations in foveal development. Indeed, a blunted or absent foveal pit is often seen in individuals born prematurely.[13] Differences in foveal morphological parameters (hereafter, foveal traits) have also been reported between males and females and among individuals with different ancestral backgrounds.[7,14,15]

Previous studies have sought to investigate the genetic architecture of OCT-derived retinal traits, including central retinal thickness, and inner and outer retinal layer thickness.[16–21] However, to date, a comprehensive analysis of the genetic determinants of foveal morphology has not been undertaken. Here, we sought to address this knowledge gap and to explore the association between foveal traits and common retinal conditions (Fig.1).

RESULTS

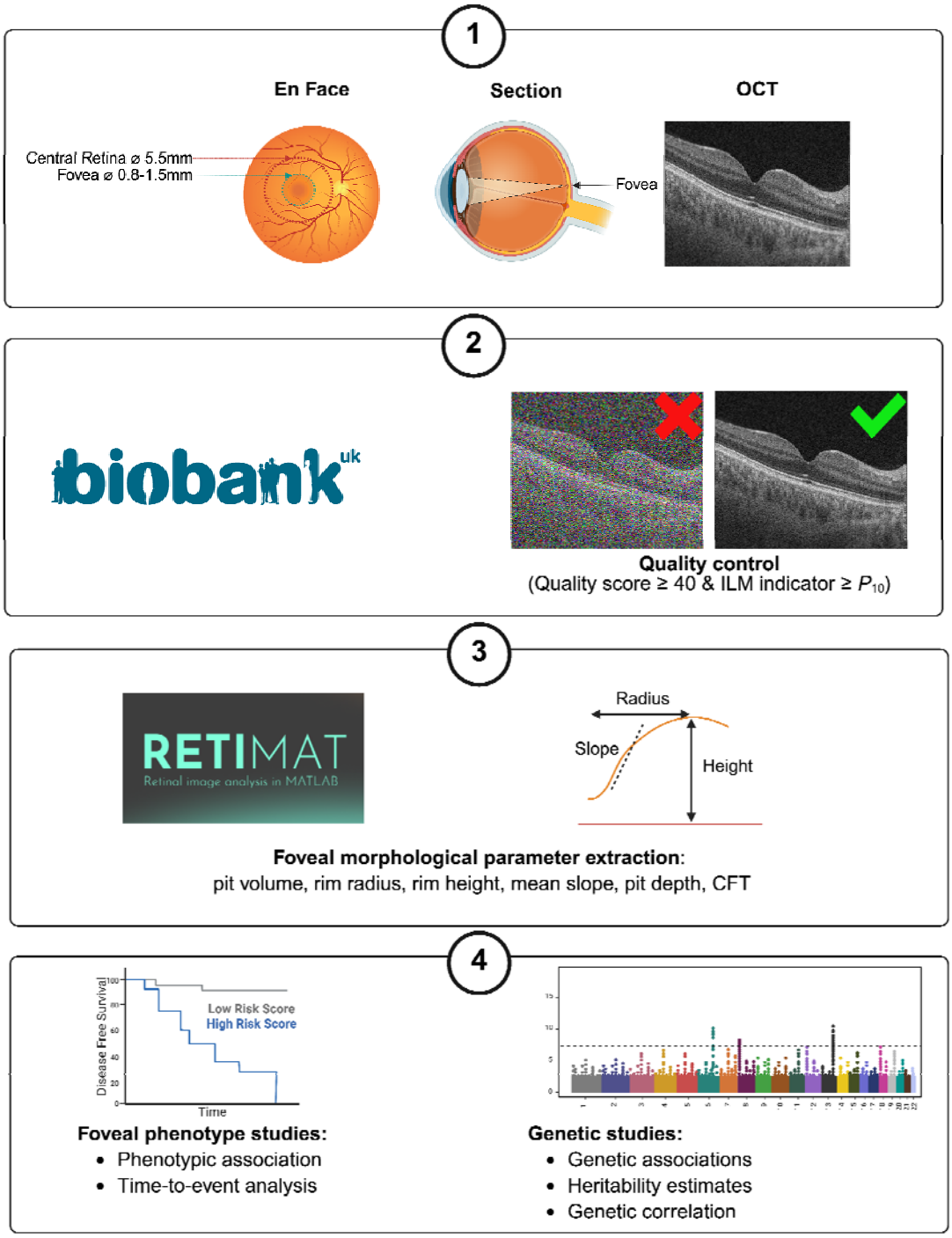

Fig.1. Outline of the study design. First, we used the RETIMAT tool to extract six key foveal traits from UK Biobank OCT scans (pit volume, rim radius, rim height, mean slope, pit depth and CFT). Subsequently, we performed phenotypic and genetic studies to gain insights into these foveal traits. Phenotypic analyses included the investigation of

the relationships between the studied foveal traits and age, spherical equivalent refractive error, sex, genetic ancestry, and visual acuity. Time-to-event analyses involved assessing the relationships between the six studied foveal traits and two major causes of visual impairment, age-related macular degeneration and glaucoma. Genetic investigations included common-variant genome-wide association studies (primary and replication), rare-variant burden tests, heritability estimation, and genetic correlation analyses.

OCT, optical coherence tomography; CFT, central foveal thickness.

Phenotypic variability in foveal traits

After applying standard OCT quality control filters[21], we defined a subset of the UK Biobank population with high-quality OCT scans (see Methods section for further details). Restricting this subset to unrelated individuals yielded a cohort of 39,521 participants with an age and sex profile similar to that of the overall UK Biobank population.[16] Most study subjects were female (52%) and the mean age at OCT imaging was 57.9 years (standard deviation: 8.1 years).

For each study subject, an OCT ‘volume scan’ (containing 128 cross-sectional images) was available from the central retina of each eye. These scans were processed using RETIMAT, an automated pipeline designed to extract foveal traits from OCTs.[15] We analysed both eyes but focused primarily on the left eye as it was imaged second and showed slightly higher image quality on average.[5,19] Six foveal parameters were assessed: foveal pit volume, rim radius, rim height, mean slope, pit depth and central foveal thickness (CFT) (Fig.1 and Table 1). The greatest fold range across UK Biobank participants was observed for pit volume (14.9-fold), followed by pit depth (6.3-fold) and mean slope (6.0-fold), indicating large differences between the most extreme phenotypes in the

population. In contrast, parameters such as rim height (1.3-fold), rim radius (2.1-fold), and CFT (3.0-fold) were more constrained (Fig.2).

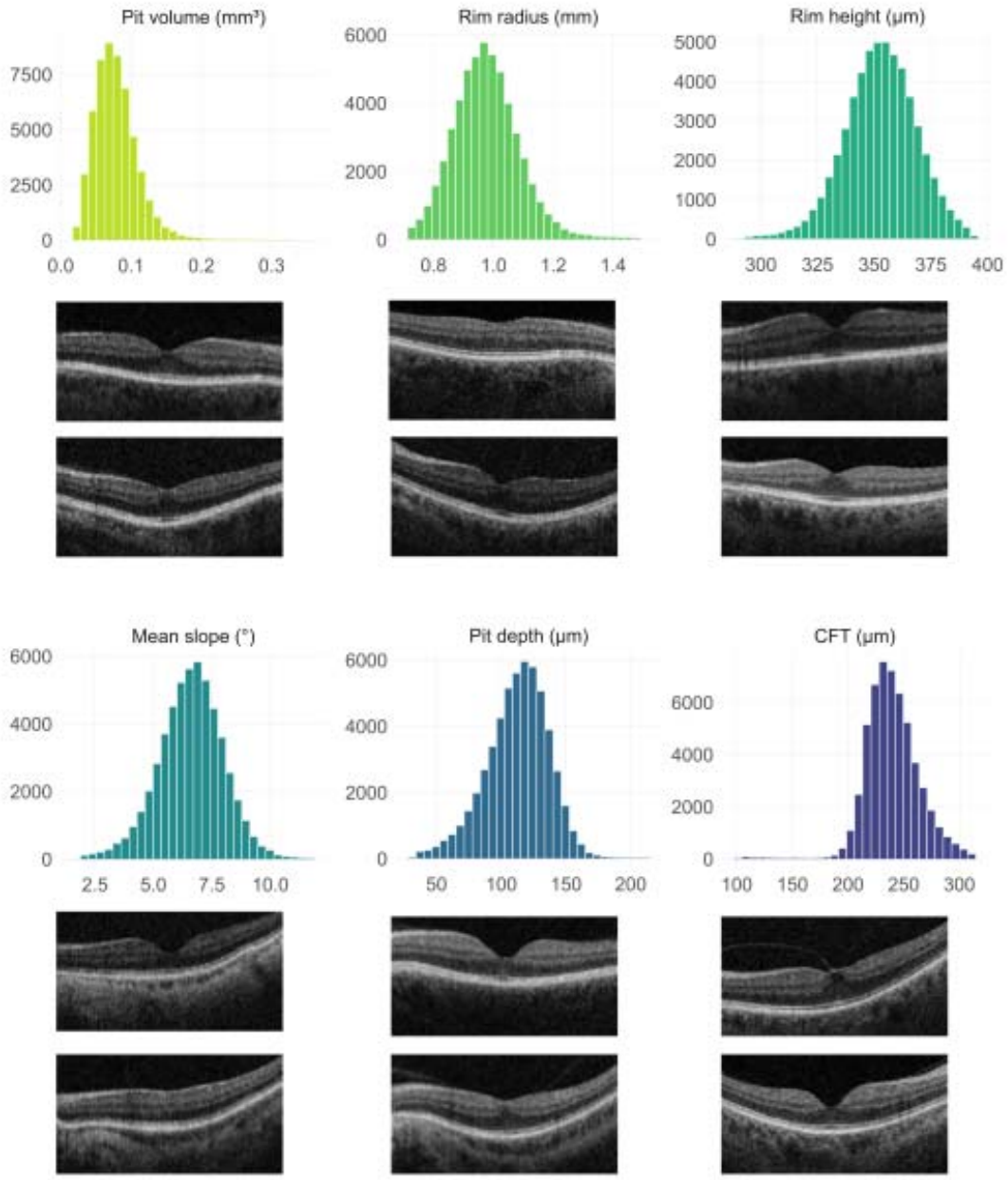

Fig.2. Histograms showing the distribution of six foveal traits in UK Biobank participants (left eyes; after removal of 1% from the upper and lower tails of the data). Also shown are six examples of OCT scans from the extreme ends of each distribution. The following mean values were obtained: pit volume 0.079 mm^3 (range:

0.024–0.352 mm^3), rim radius 0.98 mm (range: 0.71–1.48), rim height 353 µm (range: 291–394 µm), mean slope 6.62° (range: 1.93–11.6°), pit depth 113 µm (range: 33.4–209 µm), central foveal thickness (CFT) 240 µm (range: 104–312 µm). A summary of the mean and median values for all traits are provided in Supplementary Tables S2 and S3.

Table 1. Definitions of the six RETIMAT-derived foveal traits analysed in this study

Foveal trait	Definition
Pit volume (mm^3)	Integrated volume between rim height and the full thickness profile
Rim radius (mm)	Radial distance from centre to point of rim height
Rim height (µm)	Maximum thickness at the foveal rim
Mean slope (°)	Average inclination from centre to rim
Pit depth (µm)	Rim height minus central foveal thickness
Central foveal thickness (µm)	Thickness at the foveal centre

A pictorial representation of rim radius, rim height and mean slope can be found in Fig.1.

We next used multivariable linear regression models to assess how key demographic and ophthalmic factors relate to foveal morphology (Fig.3). Across traits, spherical equivalent refractive error showed modest associations and generally small effect sizes. In contrast, sex had a clear and consistent influence on foveal traits: female sex was associated with greater pit volume, rim radius and pit depth. Genetic ancestry also accounted for substantial variation; individuals of African ancestries differed from their European counterparts in several traits and, on average, had larger pit volume, rim radius, and pit depth. Taken together, these results highlight sex and ancestry as key drivers of inter-individual variability in foveal morphology, with spherical equivalent and age having more modest effects (Supplementary Table S1). Additional summary data showing the differences in foveal traits between different sex and ancestry groups are provided in Supplementary Table S2 and Supplementary Table S3.

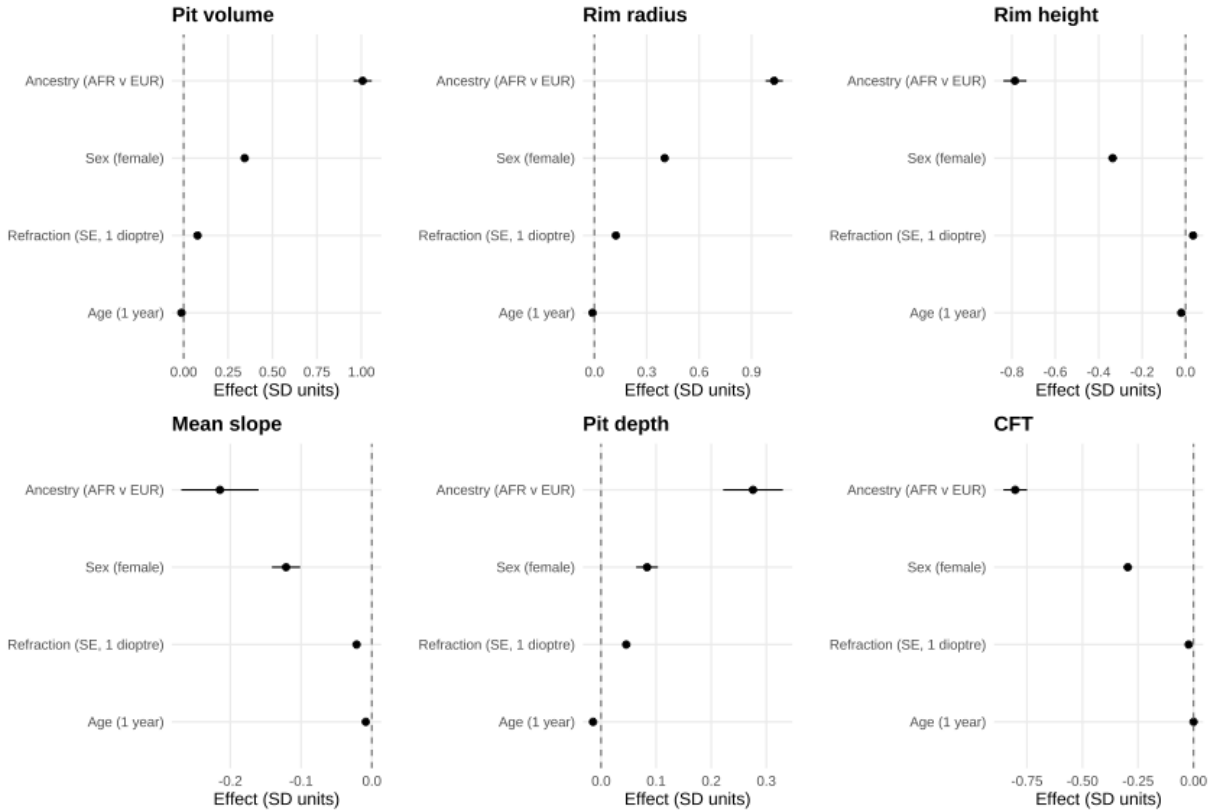

Fig.3. Forest plots showing the results of multivariate linear regression analyses for foveal traits in relation to key participant characteristics (genetic ancestry, sex, refractive error and age). Each panel shows the effect estimates from linear regression models fitted separately for the six foveal traits. Points represent regression coefficients, with horizontal bars indicating 95% confidence intervals. Sex and ancestry showed the largest and most consistent effects across traits, while age and refractive error exhibited comparatively smaller influences. Full numerical results are provided in Supplementary Table S1. While this analysis used left-eye scans, averaging measurements from both eyes produced comparable results (Supplementary Fig. S1).

Aiming to gain insights into the factors underlying the detected differences between ancestral groups, we investigated the role of fundus (principally choroidal) pigmentation. To evaluate this, we used a fundus imaging-derived proxy of pigmentation, the 'Retinal Pigment Score' (RPS).[22] We then calculated the unique variance explained (adjusted R^2) values by RPS and ancestry across the six studied foveal traits, adjusting for age, sex and spherical equivalent refractive error. Overall, genetic ancestry explained a greater proportion of trait variance than fundus pigmentation for most traits, particularly pit volume and rim radius. It is noted that pigmentation explained negligible unique variance for rim radius, suggesting little independent contribution beyond genetic ancestry (Fig.4; Supplementary Table S4).

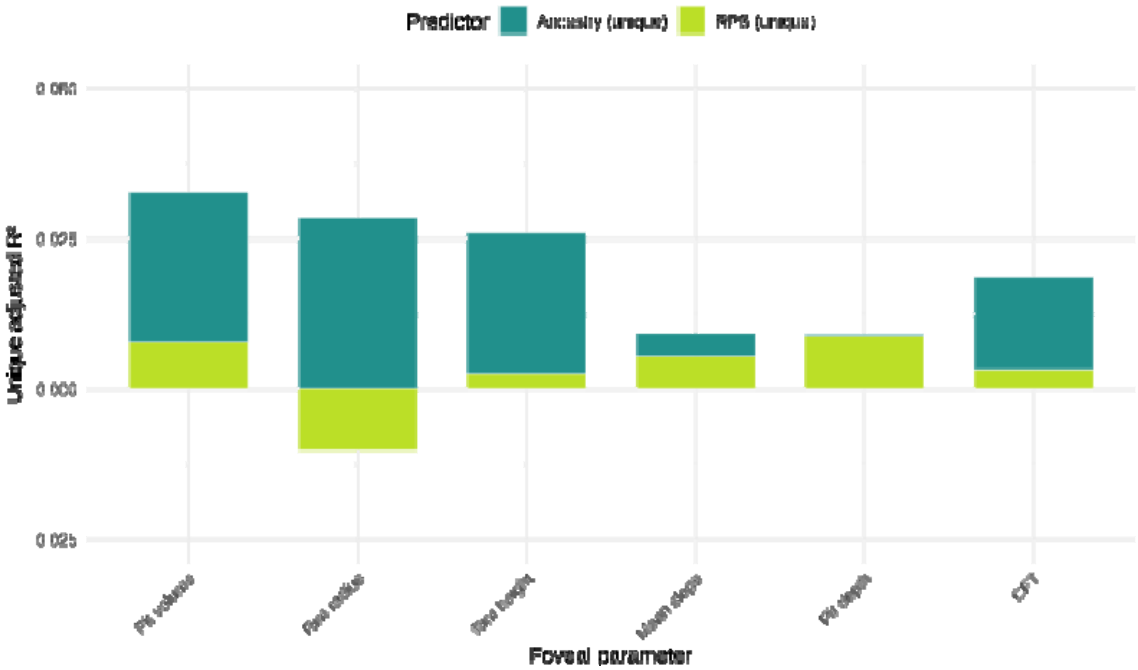

Fig.4. Unique contributions of fundus pigmentation and genetic ancestry to foveal morphology (left eye). Bar plots show the unique adjusted R^2 values for the six studied foveal traits, representing the proportion of variance explained by Retinal Pigment Score

(RPS) and genetic ancestry, after adjusting for age, sex and spherical equivalent refractive error. Unique R^2 values were calculated from linear models by subtracting the R^2 of ancestry-only or RPS-only models from the combined model. Genetic ancestry alone explained a modest but consistent proportion of variance across most traits, with the largest unique contributions observed for rim radius (2.3%), pit volume (1.9%), and rim height (2.0%). Smaller effects were seen for CFT (1.3%), mean slope (0.3%), and pit depth (0.05%). In comparison, RPS alone accounted for additional variance to a lesser extent, with its largest contributions observed for pit depth (1.0%), mean slope (0.6%), pit volume (0.5%), and CFT (0.4%). For rim radius, the unique RPS contribution was slightly negative, which likely reflects modelling noise rather than a meaningful inverse relationship. Full numerical results are provided in Supplementary Table S4.

To assess the extent to which foveal morphology predicts visual acuity, we performed linear regression with LogMAR vision as the outcome, and age, sex, spherical equivalent refractive error, and genetic ancestry as covariates. All six foveal traits showed statistically significant associations with acuity except central foveal thickness, but in every case the effect sizes were small (model R^2 values ranged from 2.8–3.0%). Mean slope was the strongest predictor, with flatter slopes associated with worse vision. Full effect estimates and confidence intervals are provided in Supplementary Fig. S2.

Association between foveal traits and risk of retinal disease

To investigate whether foveal morphology constitutes a risk factor for future retinal conditions, we performed Cox proportional hazards modelling using the six studied foveal traits, along with time-to-event data for two leading causes of visual impairment, AMD and glaucoma. We adjusted for age, sex, spherical equivalent refractive error, and genetic ancestry in these analyses.

For AMD (n=959 cases), significant associations were observed with larger pit volume (hazard ratio [HR] per one standard deviation [SD] 1.09; 95% confidence interval [CI] 1.04–1.16; p = 0.026). For glaucoma (n=844 cases), there were statistically significant protective effects for mean slope (HR per SD 0.90; 95% CI 0.84–0.96), rim height (HR per SD 0.83; 95% CI 0.77–0.89), and pit depth (HR per SD 0.87; 95% CI 0.82–0.93) (Fig.5, Supplementary Table S5).

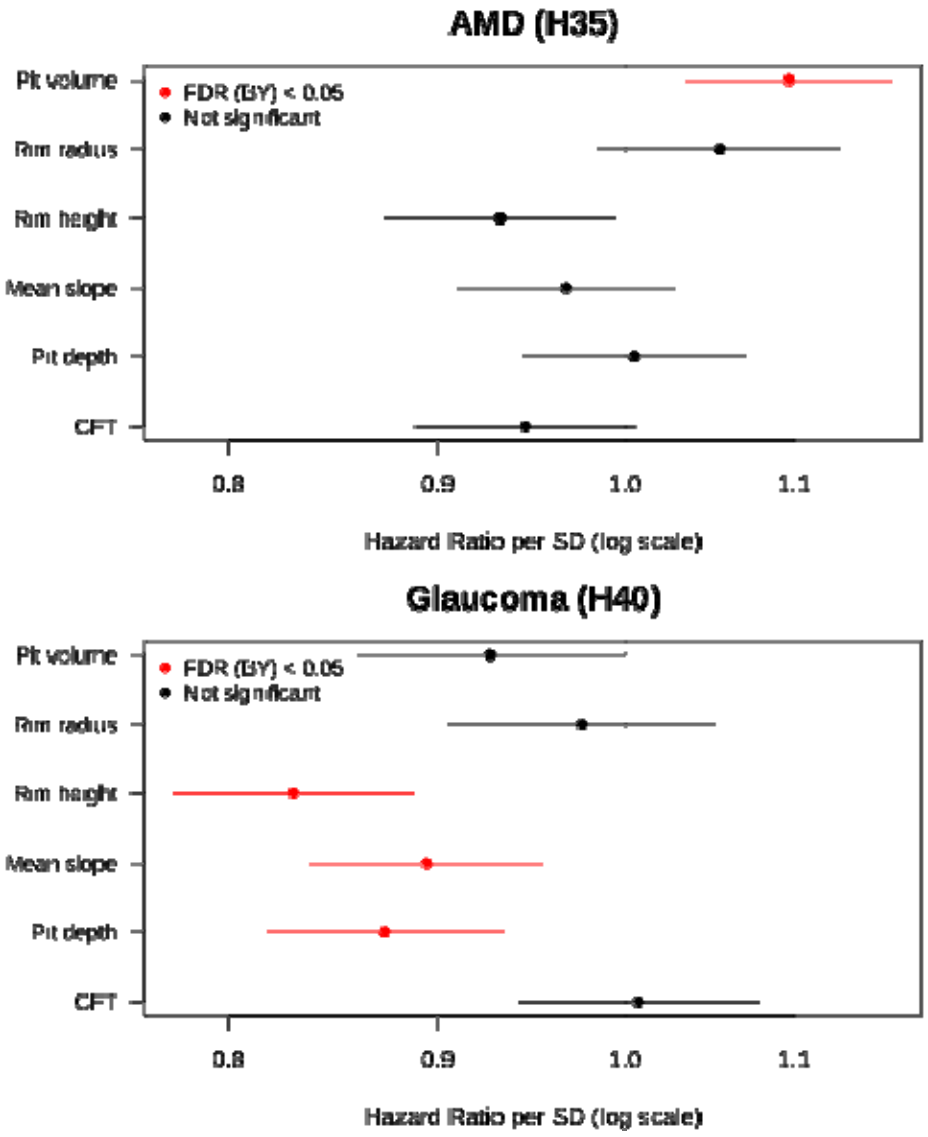

Fig.5. Cox regression analysis of the associations between foveal traits and post-OCT-scan assigned codes for AMD (H35) and glaucoma (H40). Statistically significant

associations (after correcting for multiple comparisons using a 5% false-discovery rate [FDR] Benjamini–Yekutieli [BY] threshold) are highlighted with red. Further information, including numerical data, can be found in Supplementary Table S5. While this analysis used left-eye scans, averaging measurements from both eyes produced comparable results (Supplementary Fig. S3).

AMD, age-related macular degeneration; CFT, central foveal thickness; SD, standard deviation; OCT, optical coherence tomography.

Genetic associations of foveal traits

To investigate the genetic factors influencing the six studied foveal traits, we performed common-variant genome-wide association studies (GWAS) using REGENIE.[23] For these analyses, we defined a subset of the UK Biobank population that can be considered genetically well-mixed (*i.e.* includes participants that were assigned by genotype principal component analysis to a cluster with subjects of mostly European-like ancestries). After applying relevant imaging, genetic, and foveal trait quality controls, this cohort included 36,205 individuals; 29,710 of these were recruited between 2006 and 2010 (Instance 0, ‘Initial assessment’) and were used in the primary analysis while 6,495 were independently recruited between 2012 and 2013 (Instance 1, ‘First repeat assessment visit’) and were included in the replication study. The following covariates were incorporated into the models: age, sex, height, weight, spherical equivalent refractive error, and genetic principal components 1 to 20. A study-wide threshold ($p < 8.3 \times 10^{-9}$) was used to account for the different association routes that were utilized; this was obtained after applying Bonferroni correction for six tests to the conventional $p < 5 \times 10^{-8}$ ‘genome-wide significance’ threshold.

Genome-wide significant variants in the primary GWAS included: 5,023 for pit volume; 5,234 for rim radius; 6,730 for rim height; 3,457 for mean slope; 4,006 for pit depth; and 2,387 for CFT. Following analysis with GCTA-COJO (conditional and joint multiple-variant analysis),[24] these merged into the following lead loci: 54 for pit volume, 56 for rim radius, 35 for rim height, 27 for mean slope, 35 for pit depth, and 23 for CFT (Fig.6, Supplementary Fig.S4-9; Supplementary Dataset S1). We subsequently performed a replication GWAS using UK Biobank subjects that were not included in the primary analysis, establishing a high level of concordance between the primary and replication studies (with all traits having a correlation coefficient greater than 0.9; Supplementary Fig.S10–15). Although the replication sample was considerably smaller, several lead loci still reached genome-wide significance in both studies: 6 for pit volume, 3 for rim radius, 1 for rim height, 1 for mean slope and 1 for pit depth (Supplementary Dataset S1).

We identified a combination of trait-specific and shared loci influencing foveal morphology. Many of these loci encompass variants previously linked to retinal layer thickness parameters (including *TSPAN10* and *LINC00461*) while a subset of them has been linked to monogenic disorders, most notably, albinism (including *TYR*, *OCA2* and *GPR143*) (Table 2 and Supplementary Dataset S1). Furthermore, our primary analysis identified several lead signals that have not been previously linked with retinal phenotypes (including variants at the *CYP1A1* and *KMT2A* loci). We also detected multiple lead variants for which associations

have only been detected for retinal thickness measurements but not for foveal/macular traits (including at the *FGFR2* and *SPRY2* loci).

MAGMA gene set enrichment analysis did not yield any statistically significant hits after correction for multiple testing. We note that the genomic inflation factors (λGC) ranged from 1.12 to 1.17, with corresponding linkage disequilibrium (LD) score intercepts close to 1 (range: 1.005–1.027). These results suggest minimal confounding from population structure or cryptic relatedness. The attenuation ratios were uniformly low (all < 0.11), consistent with polygenic architecture and well-controlled inflation across all six studied traits (Supplementary Table S6).

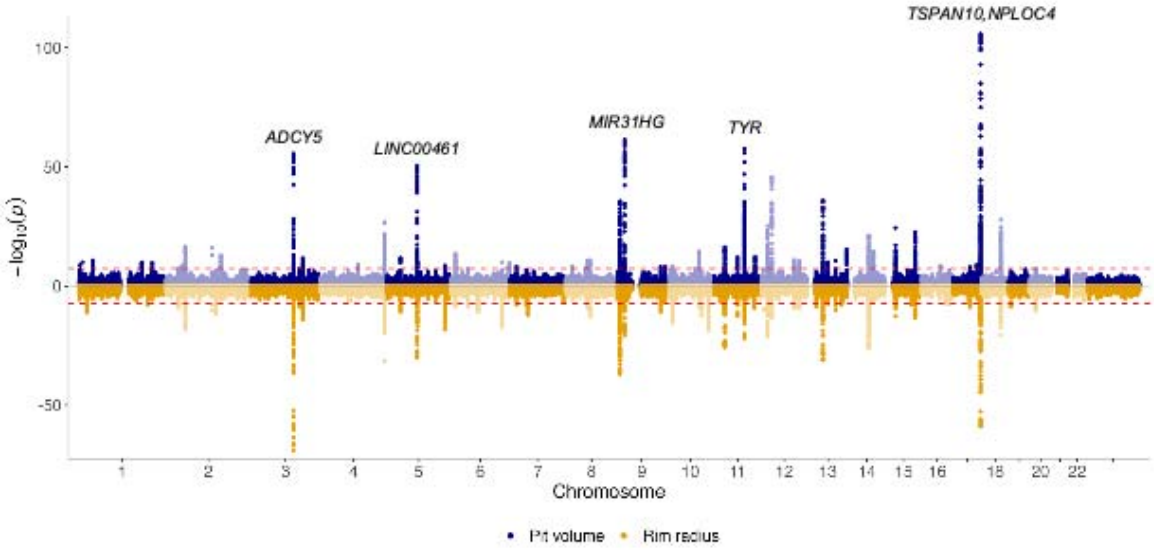

Fig.6. A Miami plot, illustrating the results of the primary genome-wide association study for foveal pit volume (top) and rim radius (bottom) (left eye). The red line indicates the threshold for genome-wide significance, and 5 key loci exceeding this value have been annotated.

In addition to the above common-variant GWAS, we performed a rare variant burden analysis using REGENIE.[23] This identified genome-wide significant associations between *SIX6* and both pit depth and pit volume ($p < 4.6 \times 10^{-}$□).

Heritability estimates for foveal traits

We used linkage disequilibrium (LD) score regression analysis[25] to obtain heritability estimates for the six studied foveal traits. We found moderate to high heritability, ranging from $h^2 = 0.29$ (standard error [SE] = 0.03) for CFT to $h^2 = 0.43$ (SE = 0.04) for pit volume. Rim height ($h^2 = 0.41$), rim radius ($h^2 = 0.39$), pit depth ($h^2 = 0.34$), and mean slope ($h^2 = 0.31$) were also significantly heritable (Supplementary Table S6).

Global genetic correlation between foveal traits

LD score regression was also used to assess the global genetic correlation between the studied traits. Because the six foveal traits capture related aspects of macular architecture, we expected some degree of phenotypic correlation. We therefore used LD score regression to quantify the extent of shared genetic architecture and to determine whether relationships between traits simply reflected measurement interdependence or suggested deeper biological overlap. We found significant interdependence between many foveal traits. The strongest correlations (rg > 0.8) were observed between pit depth and mean slope (rg = 0.88) and between pit volume and rim radius (rg = 0.85), suggesting that these pairs reflect closely related biological processes. Moderate correlations (rg = 0.6-

0.8) included pit depth and pit volume (rg = 0.76), mean slope and rim height (rg = 0.65), and pit depth and rim height (rg = 0.57), indicating shared underlying variation across several morphological aspects of the fovea.

In contrast, correlations between CFT and other parameters were more variable. We observed strong negative correlations between CFT and pit volume (rg = –0.79), pit depth (rg = –0.69), and rim radius (rg = –0.51), consistent with an inverse relationship between retinal thickness and pronounced foveal pit excavation (Fig.7).

Correlations between foveal traits and fundus pigmentation (RPS) were generally weak (rg = -0.23 with pit depth, -0.22 with mean slope), with the strongest positive correlation seen with CFT (rg = 0.23) (Supplementary Table S7).

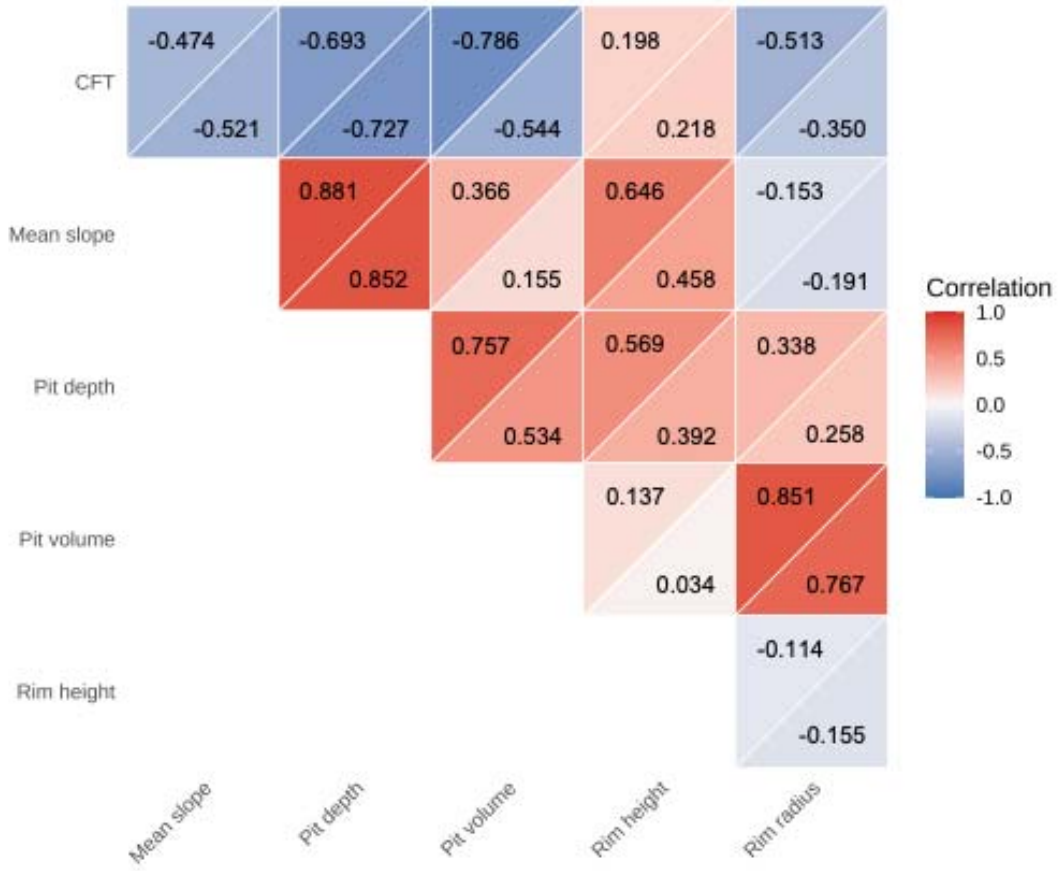

Fig.7. Genetic and phenotypic correlations between foveal traits. The upper triangle of each cell contains the phenotypic correlation coefficient for each trait-trait pair, whereas the lower triangle contains the corresponding genetic correlation coefficient. The observed correlation patterns are consistent with expected geometric relationships and shared genetic influences (rather than arising solely from measurement covariance). Further information, including numerical data, can be found in Supplementary Table S7.

CFT, central foveal thickness.

Table 2. Summary of the 10 top-ranking loci associated with foveal traits**.**

Top-ranking common variant in locus	Chr: position (GRCh37)	Key gene(s)	Allele freq	Foveal trait with significant result (minimum p-value)	Selected previous associations in the GWAS Catalog; [Panelapp association(s)]
rs6420484	17:79612397	*TSPAN10 / NPLOC4 / PDE6G*	0.65	Pit depth (2.01×10^{-107}); Pit volume (7.41×10^{-105}); Rim radius (3.54×10^{-59}); Mean slope (3.16×10^{-55}); Rim height (4.88×10^{-48})	Retinal thickness measurements, refractive error, eye colour, hair colour
rs3138142	12:56115585	*RDH5 / CD63*	0.24	Rim height (1.98×10^{-77}); Pit depth (2.86×10^{-14}); Mean slope (6.21×10^{-13})	Retinal thickness measurements, refractive error, retinal vascular fractal density; [retinal dystrophy]
rs11708067	3:123065778	*ADCY5*	0.24	Rim radius (6.34×10^{-69}); Pit volume (7.95×10^{-56})	Retinal thickness measurements, height, birth weight, type 2 diabetes, glucose levels, HbA1c levels, cholesterol levels; [dyskinesia]
rs1042602	11:88911696	*TYR*	0.37	Pit depth (1.67×10^{-62}); Pit volume (8.26×10^{-58}); Rim radius (1.16×10^{-22}; Mean slope (3.48×10^{-39}); CFT (9.32×10^{-40});	Retinal thickness measurements, brain measurements, skin colour, hair colour; [albinism]
rs9298817	9:21576591	*MIR31HG*	0.66	Pit volume (1.43×10^{-61}); Rim radius (1.44×10^{-21}); Rim height (2.30×10^{-20})	Retinal thickness measurements, thyroid medication use
rs17421627	5:87847586	*LINC00461*	0.07	Pit volume (3.12×10^{-46}); CFT (1.34×10^{-35}); Rim radius (3.87×10^{-32}); Rim height (1.60×10^{-27})	Retinal thickness measurements, retinal vascular fractal density
rs11051145	12:31050201	*TSPAN11*	0.16	Pit volume (5.02×10^{-46}); CFT (5.22×10^{-34})	Retinal thickness measurements, optic disc size

rs7020703	9:8632149	*PTPRD*	0.22	Rim radius (1.25×10^{-37})	Retinal thickness measurements, bone mineral density, height, restless leg syndrome
rs67138036	4:187683202	*FAT1*	0.26	Rim radius (4.58×10^{-37})	Retinal thickness measurements; [microphthalmia/ coloboma, nephropathy]
rs1493523	15:44345614	*CCDC122*	0.68	Pit volume (1.86×10^{-36})	-

CFT, central foveal thickness

Mendelian randomization

We performed Mendelian randomization (MR) analysis on the foveal traits that we found to be associated with AMD or glaucoma risk. This was conducted to determine whether these associations reflected potential causal effects rather than confounding or reverse causation. The MR analysis revealed causal relationships between foveal morphology and AMD risk, but not glaucoma risk. Pit volume was causally linked to increased risk of AMD, with a wide confidence interval (inverse-variance weighted [IVW] $p = 0.03$, OR ≥ 1.32) (Supplementary Figs.S16 and 17 and Supplementary Table S8). This result was supported by a significant MR Egger ($p = 0.049$). Leave-one-out analysis indicated that four variants (Supplementary Table S9) had notable influence on the findings; however, none of these variants were identified as an outlier by Radial MR or found to be associated with confounding variables in the Open Targets resource.[26]

Recognising that our analyses may be impacted by the correlated nature of foveal traits, we conducted multivariable MR considering the causal relationship between all six foveal traits and AMD. Analysis of the multivariable model revealed significant risk of pleiotropy (Q-statistic p-value = 4.0×10^{-8}), and evidence of weak instruments for pit volume (F-statistic = 3.92), mean slope (F-statistic = 2.08), rim radius (F-statistic = 2.59) and pit depth (F-statistic = 4.56). Overall, the multivariable analysis (using conventional IVW and Q-statistic

minimization) was likely underpowered, limiting the ability to detect significant associations.

Overall, these findings provide evidence that pit morphology causally influences the risk of AMD but not that of primary open-angle glaucoma. Although the univariate MR results suggest that the leading causal trait is pit volume, the correlation between foveal parameters and the weak instrument bias in multivariable MR mean that it remains possible that other foveal morphological traits could be important. Notably, in all analyses, there was no evidence of reverse causation.

DISCUSSION

In the present study, we performed large-scale phenotypic and genetic analyses to better understand the variability and determinants of foveal morphology. By leveraging retinal imaging data from UK Biobank participants and a comprehensive foveal trait calculation tool (RETIMAT), we were able to detect differences in foveal morphology influenced by sex, genetic ancestry, and genetic factors. We also found a notable association between foveal pit volume and AMD.

We first analysed how foveal architecture varies at the population level. As the number of subjects in this study is an order of magnitude greater than in most prior reports, we were able to identify previously unrecognized variability in foveal

pit morphology (e.g. 15-fold for pit volume). Sex and ancestry were found to significantly influence foveal morphology, an observation that is in keeping with the findings of previous smaller-scale studies.[7,9,14,15] In line with previous research, males exhibited greater rim height, shorter rim radii, and a steeper mean slope.[15] Similarly, we found that individuals with African ancestries had wider, deeper, and more voluminous foveal pits than their European counterparts, in line with findings by Zouache *et al.*[7] The smaller East- and South-Asian ancestral groups fell between these two, consistent with the limited normative datasets available for Asian populations.[27,28] It is highlighted that, in contrast to most previous studies, we used genetic ancestry, a metric that is more accurate and objective than ethnicity or self-reported ancestry.[29] We also performed additional analyses to gain insights into the extent to which the observed difference between continental groups is driven by pigmentation. Our observations suggest that genetic ancestry tends to be an independent contributor irrespective of fundus pigmentation, especially for foveal pit volume and rim radius.

We found that a larger pit volume is a key risk factor for AMD, and that there is a 33% increase in risk per 0.1 mm^3 increase in pit volume. This observation was supported by two independent approaches: Cox regression and Mendelian randomization. The results of the latter substantially reduce the risk that the observed association being due to reverse causation or confounding, and support the assertion that pit volume is a risk factor for AMD rather than a correlate. The hazard ratio per one SD was 1.09 (95% CI 1.04–1.16), and the

corresponding odds ratio (OR) per standard deviation was 1.10 (95% CI 1.06–1.17) (Fig.5, Supplementary Tables S5 and S10). We note that several environmental and genetic risk factors have been previously associated with AMD, including: age (OR 1.1 per year), gender (OR 1.6), smoking (OR 1.9)[30], *CFH* gene variants (e.g. homozygosity for rs1061170 corresponds to OR of 4.7)[31], *ARMS2* locus variants (e.g. homozygosity for rs10490924 corresponds to OR of 8.6)[32] and family history (OR 10.8).[33] Although AMD selectively affects the foveal/macular region, to date, anatomical risk factors have been understudied[9] and, to our knowledge, this is the first time that specific foveal morphological parameters are found to set the stage for susceptibility to AMD. It can be speculated that the link between a larger pit and AMD risk is driven by differences in the distribution of macular xanthophyll pigments and/or by alterations in photoreceptor cell densities in the vulnerable parafoveal area of low rod-to-cone ratio.[34] Future advanced ophthalmic imaging and mathematical modelling studies will provide further insights into how foveal anatomy predisposes to this leading cause of visual impairment.

Following phenotypic analyses, including of foveal traits that have received little attention so far (such as foveal volume and radius), we performed genetic association studies. We found that the observed morphological diversity has a strong genetic underpinning, with a high level of heritability across most traits (Supplementary Table S6). Pigmentation-related genes such as *TYR* and *TSPAN10* surfaced across multiple foveal traits, underscoring the role of melanin synthesis in the shared developmental pathways that shape foveal morphology

(Table 2). This is in keeping with previous observations in albinism[35,36] and in a smaller cohort where a link between the common functional *TYR:*c.1205G>A (p.Arg402Gln) [rs1126809] variant and decreased rim radius was reported.[37]

While many of the lead variants detected here have previously been linked to retinal traits, at least 130 of them have no such prior associations (Supplementary Dataset S1). Two examples are *CYP1A1* and *KMT2A. CYP1A1* (lead marker: rs200391170; association with mean slope; $p = 2.2 \times 10^{-21}$) encodes a major cytochrome P450 enzyme and is involved in the metabolism of both endogenous substances and environmental chemicals. It has been implicated in the conversion of all-trans retinol to all-trans retinoic acid in human foetal tissues.[38] Notably, retinoic acid gradients are essential for dorsoventral patterning, and retinoic acid signalling has been directly linked to the positioning of the fovea-like area in the chick retina.[39,40] *KMT2A* (lead marker: rs7948661; association with rim radius; $p = 5.9 \times 10^{-10}$) encodes a histone methyltransferase that mediates H3K4 methylation, a key epigenetic modification associated with transcriptional activation.[41] The relevant molecule regulates the expression of developmental genes across various tissues, including the developing retina, and conditional *Kmt2a* knockout in mice has been shown to lead to disrupted retinal layering.[42,43]

A subset of the detected lead variants (n=17) has been previously associated with retinal thickness measurements (either clinically-used[16–18] or deep learning based[5,20,44]) but not with foveal/macular traits (Supplementary Dataset S1).

These novel associations reported here enhance the interpretability of the relevant signals and allow more robust links to be drawn with central retinal development/patterning. Two notable examples are *FGFR2* and *SPRY2. FGFR2* (lead marker: rs146727842; association with mean slope; $p = 1.4 \times 10^{-20}$) encodes a receptor tyrosine kinase that is essential for embryonic development.[45] *FGFR2* has been shown to interact with *FGF8*, whose expression is required to pattern the chick fovea-like region.[39,40,46] *SPRY2* (lead marker: rs7996082; association with rim radius; $p = 9 \times 10^{9}$) encodes a member of the Sprouty family of proteins, which act as negative regulators of the FGF signalling pathway.[47] Experimental evidence from murine models suggests a prominent role for *SPRY2* in eye development.[484539,40,4617,4950]

This study has several limitations. First, obtaining accurate quantitative measurements of OCT-derived retinal features is inherently challenging. One issue is image scaling, as precise measurements require knowledge of the exact lateral scale of each scan. To address lateral magnification, we included spherical equivalent refractive error as a covariate in our analyses. Although this approach is less precise than using ocular axial length[33,51], it represents a pragmatic alternative given that axial length measurements are not available within UK Biobank. This analytical framework closely aligns with most previous genetic association studies involving retinal imaging-derived phenotypes.[16,17,19–21], and, reassuringly, the findings of our phenotypic analyses showed good agreement with those from independent, smaller, more targeted studies.[52,53] To evaluate whether the use of refractive error in this context influenced our time-to-

event results, we performed sensitivity analyses excluding participants at increasingly strict spherical equivalent thresholds (±6, ±2, ±1 dioptres). The hazard ratios remained stable throughout (Supplementary Table S11). Second, we relied on UK Biobank healthcare record data to identify cases of AMD and glaucoma. These records are known to be incomplete, and several alternative methods using retinal imaging data have been proposed.[54,55] Although these have shown positive diagnostic performance, they can overestimate prevalence,[55] and we opted to use a conventional approach focused on record-based diagnoses. Finally, while the UK Biobank was designed to be broadly representative of the ageing UK population, it is subject to selection biases. All reported associations should therefore be interpreted considering this limitation.[56,57]

In conclusion, we show that (i) foveal architecture is patterned by sex, genetic ancestry and genes related to pigmentation, and (ii) one aspect of that architecture, pit volume, appears to lie on the causal pathway to AMD. These findings position foveal pit metrics as potential biomarkers of macular vulnerability and invite mechanistic work to dissect how developmental pathways intersect with ageing to drive retinal degeneration.

MATERIALS AND METHODS

Ethical approval

The UK Biobank has received approval from the UK National Information Governance Board for Health and Social Care and the National Health Service North West Centre for Research Ethics Committee (Ref: 11/NW/0382). This research was conducted using the UK Biobank Resource under projects 53144 and 49978. All investigations were conducted in accordance with the tenets of the Declaration of Helsinki.

UK Biobank: cohort characteristics and ophthalmic phenotyping

We used data from the UK Biobank, a resource containing genomic and health information from 502,355 individuals from across the United Kingdom, aged between 40 and 69 years at the time of recruitment.[3] Subsets of UK Biobank volunteers underwent enhanced phenotyping including visual acuity testing (>130,000 individuals), non-cycloplegic autorefraction (>125,000 individuals) and imaging of the central retina using colour fundus photography and OCT (>84,000 individuals). Baseline ophthalmic assessment was conducted between 2009 and 2010 for most participants and between 2012 and 2013 for a smaller subset.[4]

Best-corrected visual acuity was assessed using a computer-displayed LogMAR chart (Precision Vision, LaSalle, IL, US) (UK Biobank data-fields: 5208 and 5201). Participants wore their habitual distance correction and were tested at 4m; if unable to identify any letters, the chart was moved to 1m. Starting from the top line, testing stopped once ≥2 letters on a line were misread.[4]

Non-cycloplegic autorefraction was carried out using a Tomey RC 5000 device (Tomey Corp., Nagoya, Japan). The spherical equivalent refractive error (spherical error + 0.5 ×

cylindrical error) was subsequently calculated for each participant (data-fields 5084-5085; 5086-5087).[4]

Colour fundus photographs and spectral-domain OCT images were acquired using the Topcon 3D-OCT 1000 Mark II device (Topcon Corp., Tokyo, Japan), without pharmacological dilation (data-fields 21015, 21016, 21011, 21013). OCTs were obtained using a ‘3D macular volume’ protocol (6 × 6 mm; 128 horizontal B-scans, each comprising 512 A-scans arranged in a raster pattern).[5,44,58] The right eye was imaged first. Our analyses predominantly focused on left eye images as familiarity with the test generally yielded higher-quality scans.[5,19] For robustness, an average value for each foveal trait (calculated using both left and right eye measurements but falling back to the single available eye when only one scan passed QC) was used in a subset of phenotypic analyses (Supplementary Fig.S1 and S3). Comparisons of foveal traits in the left, right, and averaged datasets are presented in Supplementary Table S12).

Fundus pigmentation quantification

We used a recently described method[22] to evaluate fundus pigmentation in UK Biobank participants. This involved calculating the Retinal Pigment Score (RPS), a continuous quantitative metric that is thought to primarily reflect choroidal pigmentation.[59]

RPS was derived using the approach described by Rajesh *et al*. which entails selecting fundus photographs of sufficient quality (*i.e.* those labelled as ‘Good’ by Automorph, an established deep learning tool)[60] and processing them through the RPS pipeline to quantify background pigmentation.[17]

OCT quality control and foveal morphological parameter extraction

OCT scans were filtered for overall quality in line with previous studies.[19,21] Briefly, we discarded OCTs that (j) had a quality score below 40 and (ii) fell within the lowest 10% of the inner limiting membrane (ILM) edge-strength indicator (a metric that captures the sharpness and continuity of the ILM boundary and flags blinks, signal dropouts, and major segmentation errors).[21] Where multiple scans were available per instance, only the primary (index 0) image was used as quality metrics are not provided for additional scans.

OCT images meeting the above quality control criteria were processed using RETIMAT, an open-source MATLAB toolbox for OCT image analysis. The processing pipeline included the following steps:

- parsing Topcon (.fda) files to extract the ILM and Bruch's membrane (BM) surfaces delineated by the device software;
- computing total retinal thickness maps;
- automatically aligning thickness maps to the foveal centre;
- transforming raster thickness maps into a radial pattern; and
- computing morphometric values.

RETIMAT has been used successfully in previous studies and its fully automated methods for fovea location and analysis have been independently assessed, making it well-suited for high-throughput analyses.[15,61] It is noted that RETIMAT functions primarily as a utility rather than as a segmentation algorithm. It does not perform any image segmentation or grading itself, and instead operates entirely on the ILM–BM boundaries supplied by the Topcon device. These particular boundaries are among the most robust OCT features to segment due to their distinct intensity gradients, making systematic

segmentation errors unlikely. We focused on six RETIMAT-derived foveal traits: foveal pit volume, rim radius, rim height, mean slope, pit depth and central foveal thickness (CFT) (Fig.1, Table 1).

Aiming to study the phenotypic variability of these parameters, we assembled a broad 'phenotypic analysis' cohort. This included unrelated UK Biobank participants whose OCT scans passed the imaging quality control criteria for this study; whose RETIMAT-derived foveal trait values did not fall in the 1% upper or lower extreme; and who were assigned to one of the four main genetically-inferred ancestral groups (EUR, AFR, SEA, and SAS; see 'Genetic ancestry assignment' section below). Aiming to study the genetic architecture of foveal traits, a second, more focused 'genetic analysis' cohort was defined. This was limited to unrelated participants of European-like ancestries with OCT scans; no sex chromosome aneuploidy; and not flagged as outliers for heterozygosity nor missingness. Individuals with RETIMAT-derived foveal trait values exceeding 2.5 standard deviations were also excluded (Supplementary Fig.S18); this cut-off was selected in accordance with the approach used in previous genetic association studies of retinal thickness measurements.[16,17,19–21] The final GWAS sample comprised 36,205 unrelated individuals with European-like ancestries (29,710 primary plus 6,495 replication); the broader phenotypic cohort totalled 39,521 individuals across ancestries.

Genetic ancestry assignment

To facilitate inter-ancestry analyses of foveal traits, we sought to characterize the genetic ancestry of UK Biobank participants. A subset of 409,373 participants with European-like ancestries is readily available (data-field 22006) and we aimed to obtain genetic ancestry estimates for the remaining 78,296 individuals. Using a previously

described approach[62] we projected these UK Biobank participants onto reference genetic data from the 1000 Genomes Project.[63] In brief, we used directly genotyped single-nucleotide variants from the UK Biobank and genetic data from the 1000 Genomes Project (Phase 3, v5a.20130502). After matching variants between these two resources, we merged the two datasets using PLINK v2.0,[64] retaining 718,487 high-quality variants. We then performed linkage disequilibrium (LD) pruning and removed regions with long-range LD, resulting in 30,320 independent variants. Ancestry proportions were estimated using ADMIXTURE (v1.3.0),[65] with four reference groups from the 1000 Genomes Project dataset: GBR (European), YRI (African), ITU (South Asian), and CHS (East Asian). Only individuals with at least 80% ancestry probability assigned to one of these four groups were retained for further phenotypic analyses.

Statistical analyses of foveal phenotypes

We characterized the independent contributions of genetic ancestry, sex, refractive error and age (at OCT acquisition) to variability in foveal morphological traits by fitting separate multivariable linear regression models for each foveal trait. Each trait was standardized (Z-scored) prior to modelling so that the regression coefficients represented the change in the trait in standard deviation (SD) units per one unit of the predictor. Regression coefficients, 95% confidence intervals, and p-values were subsequently extracted.

To quantify the contributions of fundus pigmentation (RPS) and genetic ancestry to variability in foveal morphology, we fitted linear regression models for each trait, as follows: The two predictors were analysed together given their presumed biological relationship (as pigmentation traits vary by ancestry and may capture overlapping sources of variation).

Model 1: included RPS, spherical equivalent refractive error, and sex.

Model 2 included genetic ancestry (as a categorical variable), spherical equivalent refractive error, and sex.

Model 3: included both RPS and genetic ancestry terms, along with spherical equivalent refractive error and sex.

From each model, we extracted adjusted R^2 values to assess explained variance. Unique contributions of RPS and ancestry were derived by comparing the full model against models excluding one predictor set at a time.

Finally, the association between foveal morphology and visual acuity was studied using a linear regression approach with age, sex, spherical equivalent refractive error and genetic ancestry used as covariates.

Genome-wide association studies (GWAS)

We performed a common-variant GWAS using an additive linear model in REGENIE v3.1.1.[23] To meet the normality assumptions of GWAS, we applied rank-based inverse normal transformation to any foveal traits that deviated from a normal distribution. For this analysis, we focused only on individuals of European-like genetic ancestries (data-field 22006). We performed a primary and a replication GWAS. The focus of the former was on the 67,250 individuals that were imaged at the time of their baseline visit (Instance 0, ‘Initial assessment visit (2006–2010)’). The focus of the replication study was on the 15,568 different participants that were imaged for the first time during their first repeat assessment (Instance 1, ‘First repeat assessment visit (2012–2013)’. Thus, the two analyses were performed on non-overlapping samples.

To process the imputed genotype data, we applied conventional quality control filters using PLINK2.[64] Variants were retained if they had: an imputation quality score above 0.8; a minor allele frequency (MAF) of 5% or more; and a minor allele count (MAC) of 20 or more. Variants with a Hardy-Weinberg equilibrium p-value below 1×10^{-15} were excluded, along with those with missingness greater than 10%. Individuals with more than 10% missing genotypes were also excluded.[23]

The GWAS model was adjusted for age at recruitment (data-field 21022), sex (data-field 31), height (data-field 50), weight (data-field 21002), spherical equivalent refractive error (calculated from data-fields 5085 and 5086 and defined as spherical error + 0.5 × cylindrical error), and the first 20 genetic principal components (data-field 22009). Genome-wide statistical significance was set at $p < 8.3 \times 10^{-9}$ after correcting for multiple testing across the six studied foveal traits.

To refine the obtained association signals, further analyses were performed using the GCTA-COJO tool (conditional and joint multiple-variant analysis).[24] Variants located on different chromosomes, or more than 10 Mb apart, were treated as unlinked. Lead genetic variants were then annotated using Ensembl,[66] Open Targets,[67] and GWAS Catalog[68] data (accessed on June 24, 2025). To accurately summarize the strongest signals, the LD metrics of the changes that were highlighted as lead variants by GCTA-COJO analysis and were within 1 Mb of one another were manually inspected using the LDlink tool.[69]

Rare variant burden testing

Rare variant analyses were performed using REGENIE (v2.2.4)[23] on the UK Biobank OQFE exome dataset (data-field 23157). Gene-based burden testing of rare variants

was conducted leveraging the helper files provided with the OQFE exome release for variant annotation and deleteriousness scoring. The six foveal traits and the covariates in these analyses were identical to those used in our common-variant GWAS. As in that GWAS, rank-based inverse normal transformation was applied to foveal traits with non-normal distributions.

Variant sets were grouped at the gene level based on functional annotation masks. All analyses considered variants with alternative allele frequency (AAF) ≤ 0.01 and high-confidence annotations such as loss-of-function and predicted deleterious missense variants (loss-of-function, missense (0/5), missense (5/5), missense (>=1/5)). Gene-level results were summarized to identify loci showing suggestive or significant associations after multiple testing correction Bonferroni adjustment ($p < 4.60 \times 10^{-7}$ after correcting for 18,108 genes and six traits).

LD score regression: heritability estimation and global genetic correlation analysis

The global genetic correlations between the six studied foveal traits (pit volume, rim radius, rim height, mean slope, pit depth, and CFT) and RPS were calculated using LD score regression.[70] The GWAS summary statistics for RPS were obtained from a study by Julian *at al.*[59] The analysis adhered closely to the methodology described by Bulik-Sullivan *et al.*,[70] with genetic variants filtered according to the following criteria: inclusion in HapMap3; minor allele frequency > 0.01; imputation score > 0.9, exclusion of strand-ambiguous variants; and removal of duplicated variants. LD scores were derived from the European subset of the 1000 Genomes Project dataset.[63]

LD score regression was also used to calculate heritability, λ_G (genomic inflation factor), intercept, and ratio (denoting the proportion of inflation resulting from confounding or bias) for each of the six studied foveal traits.

Cox regression analysis

We performed Cox proportional hazards regression to investigate the association between foveal traits and incident age-related macular degeneration (AMD) and glaucoma. Participants with available OCT-derived foveal traits and outcome data were included in the analysis (n = 39,521). Disease status was defined using hospital inpatient ICD-10 diagnosis fields (data-field: 41202) together with the corresponding First Occurrence algorithm fields (data-field 131182 for H35-related outcomes and data-field 131186 H40-related outcomes) to ensure complete capture of the earliest recorded diagnosis date. The earliest available date for an AMD- or glaucoma-related ICD-10 code was taken as the disease onset.

We defined disease onset as the earliest recorded date for the relevant ICD-10 code. Participants were censored at the last available follow-up date (May 31, 2022), if their imaging date was missing, or if disease onset occurred before the scan date. By the censor date, the mean age of participants was 69 years, placing the cohort well within the typical age range for AMD. As our focus was incident disease, individuals with a recorded AMD diagnosis at or before baseline were excluded, and AMD severity was not included as a covariate because it is only defined among those who already have the disease and therefore cannot inform models of AMD onset.

Cox regression models were fitted using the ‘lifelines’ Python package,[71] with time-to-event (in days) as the outcome, and foveal traits as the predictors. All models were

adjusted for age at image acquisition, sex, spherical equivalent refractive error, and genetic ancestry. Ancestry was modelled using one-hot encoded genetic ancestry categories with individuals of European-like ancestries as the reference group. Models were fit for each trait–disease pair. Hazard ratios (HR), 95% confidence intervals, and p-values were extracted. The p-values were corrected for multiple testing using the Benjamini–Yekutieli (BY) false discovery rate (FDR) method.

To enhance the interpretability of the detected associations, we performed logistic regression using a binary outcome defined as the presence or absence of disease onset after the scan date and before the censoring date (May 31, 2022). Individuals who had not developed the disease by the censoring date were treated as controls. Covariates included age at image acquisition, sex, spherical equivalent refractive error, and genetic ancestry (encoded as dummy variables). Analyses were run separately for each foveal trait. Logistic regression models were fitted using the ‘statsmodels’ Logit function in Python[72], and odds ratios (with 95% confidence intervals) and p-values were extracted.

To account for potential imprecision introduced by using spherical equivalent rather than axial length, we conducted sensitivity analyses to assess the influence of extreme refractive error. Individuals with spherical equivalent values beyond ±6, ±2 or ±1 dioptres were excluded in separate Cox regression models. For each trait–disease pair, hazard ratios from the filtered analyses were compared to those from the primary model using a Wald test applied to the difference in log-hazard ratios (with the combined standard error derived from the two independent models). This approach allowed formal assessment of whether refractive-error outliers materially affected the estimated associations.[72]

Causal inference using two-sample Mendelian randomization

Causal associations between AMD, glaucoma and the six studied foveal traits were assessed using univariable two-sample Mendelian randomization (MR).[73,74] Population overlap biases univariable two-sample MR in the direction of causation. Accordingly, the populations contributing toward traits determined to be causal were inspected to ensure that there was no overlap. Genetic instruments were selected based on $p < 5 \times 10^{-8}$ in relation to each exposure trait. Where an exposure instrument was not present in the outcome dataset, we sought to identify a suitable proxy. Proxy variants were single-nucleotide variants that were in high LD with exposure-associated variants which were not present in the outcome dataset. Proxies were identified using the Ensembl server,[66] selecting variants with an LD R^2 value of 0.9 or above. Genetic variants were clumped using an LD R^2 value of 0.001 and a genetic distance cut-off of 10,000 Kb. This was achieved using the 1000 Genomes Project European superpopulation reference panel and the TwoSampleMR PLINK clumping function.[63,64] The effects of instruments on outcomes and exposures were harmonized to ensure that the β values (*i.e.* the regression analysis estimates of effect size) were signed with respect to the same alleles. For palindromic alleles (*i.e.* alleles that are the same on the forward as on the reverse strand), those with minor allele frequency (MAF) > 0.42 were omitted from the analysis to reduce the risk of errors due to strand issues. In addition to using a range of Mendelian randomization methods and quality control measures (as detailed below), we endeavoured to remove pleiotropic instruments and outliers from the analysis. To achieve this, instruments that were more statistically significant (in terms of p-value) for the outcome than the exposure were removed. Radial Mendelian randomization,[75] an approach that detects outlying instruments, was also used for outlier identification, and outliers were subsequently removed.[75] The Cochran's Q test was performed for each analysis. The MR Egger intercept[76] was used to detect horizontal pleiotropy. The I^2

statistic was calculated as a measure of heterogeneity between variant specific causal estimates. An $I^2 < 0.9$ indicates that MR Egger is more likely to be biased towards the null through violation of the "NO Measurement Error" (NOME) assumption. Our primary analysis was a multiplicative random effects inverse variance weighted (IVW) test, which is the most efficient analysis method with valid instrumental variables.[77] It is noted that Mendelian randomization relies upon several assumptions holding true to provide an accurate assessment of causation. The core assumptions are that (i) the instrumental variables (single-nucleotide polymorphisms) utilized are associated with the exposure; (ii) the instrumental variables are not associated with the outcome via a confounder; and (iii) the instrumental variables do not impact the outcome other than through the exposure being considered (*i.e.* no horizontal pleiotropy).[77] Robust analyses are those which can provide valid causal inference under weaker assumptions than an IVW test, and are important for a complete Mendelian randomization study. Robust tests included the weighted median (robust to up to 50% of invalid instruments), weighted mode (robust to >50% of invalid instruments but assumes more variants estimate the true causal effect than estimate any other quantity), MR Egger (robust to pleiotropic effects of variants, provided the effects are independent of the variant-exposure associations) and a leave-one-out analysis using the MRE IVW method (to test for highly influential variants).[76–79] When appraising the results of a Mendelian randomization study, the confidence with which one can assert causality is influenced by both the strength of association in the primary analysis (IVW) and the range of robust tests in which the results are consistent. Where the IVW is significant but robust tests are not, this may be in keeping with causality, but under stricter assumptions of validity across the instrumental variables utilized (and therefore may warrant more cautious interpretation).

In keeping with recent methodological recommendations for Mendelian randomization, we systematically evaluated all empirically testable assumptions underpinning our analyses. This included inspection of instrument strength, assessment of heterogeneity using Cochran's Q, evaluation of directional horizontal pleiotropy via the MR-Egger intercept, and examination of the NOME assumption using the I^2 statistic. We additionally performed radial MR to identify disproportionately influential variants, removed instruments with stronger associations with the outcome than the exposure, and carried out leave-one-out analyses to confirm that results were not driven by single variants. Together, these diagnostics provide a comprehensive appraisal of the validity of our instruments and the plausibility of MR assumptions within the constraints of current best practice.

DATA AVAILABILITY

UK Biobank data are available under restricted access through a procedure described at http://www.ukbiobank.ac.uk/using-the-resource/. All other data supporting the findings of this study are available within the article (including its Supplementary Information files).

CODE AVAILABILITY

The scripts used to analyse the datasets included in this study are available at https://github.com/davidjohngreen/fovea and https://github.com/mu-biomed/retimat.

REFERENCES

1. Bringmann, A. *et al.* The primate fovea: Structure, function and development. *Prog Retin Eye Res* **66**, 49–84 (2018).

2. Provis, J. M., Dubis, A. M., Maddess, T. & Carroll, J. Adaptation of the central retina for high acuity vision: Cones, the fovea and the avascular zone. *Prog Retin Eye Res* **35**, 63–81 (2013).

3. Meyer, H. V. *et al.* Genetic and functional insights into the fractal structure of the heart. *Nature* **584**, 589–594 (2020).

4. Bycroft, C. *et al.* The UK Biobank resource with deep phenotyping and genomic data. *Nature* **562**, 203–209 (2018).

5. Chua, S. Y. L. *et al.* Cohort profile: design and methods in the eye and vision consortium of UK Biobank. *BMJ Open* **9**, e025077 (2019).

6. Bouma, B. E. *et al.* Optical coherence tomography. *Nature Reviews Methods Primers* **2**, (2022).

7. Zouache, M. A. *et al.* Comparison of the morphology of the foveal pit between african and caucasian populations. *Transl Vis Sci Technol* **9**, 1–11 (2020).

8. Tick, S. *et al.* Foveal shape and structure in a normal population. *Invest Ophthalmol Vis Sci* **52**, 5105–5110 (2011).

9. Wagner-Schuman, M. *et al.* Race- and sex-related differences in retinal thickness and foveal pit morphology. *Invest Ophthalmol Vis Sci* **52**, 625–634 (2011).

10. Dubis, A. M., McAllister, J. T. & Carroll, J. Reconstructing foveal pit morphology from optical coherence tomography imaging. *British Journal of Ophthalmology* **93**, 1223–1227 (2009).

11. De Moraes, C. G. *et al.* Interindividual variations in foveal anatomy and artifacts seen on inner retinal probability maps from spectral domain OCT scans of the macula. *Transl Vis Sci Technol* **7**, (2018).

12. Zacharias, S. *et al.* Assessing the Relationship between Foveal Cone Density, Outer Nuclear Layer Thickness and Foveal Morphology. *Ophthalmology science* **6**, (2025).

13. O'Sullivan, M. L. *et al.* Foveal differentiation and inner retinal displacement are arrested in extremely premature infants. *Invest Ophthalmol Vis Sci* **62**, (2021).

14. Olvera-Barrios, A. *et al.* Foveal Curvature and Its Associations in UK Biobank Participants. *Invest Ophthalmol Vis Sci* **63**, (2022).

15. Romero-Bascones, D. *et al.* Spatial characterization of the effect of age and sex on macular layer thicknesses and foveal pit morphology. *PLoS One* **17**, (2022).

16. Currant, H. *et al.* Sub-cellular level resolution of common genetic variation in the photoreceptor layer identifies continuum between rare disease and common variation. *PLoS Genet* **19**, (2023).

17. Currant, H. *et al.* Genetic variation affects morphological retinal phenotypes extracted from UK Biobank optical coherence tomography images. *PLoS Genet* **17**, (2021).

18. Gao, X. R., Huang, H. & Kim, H. Genome-wide association analyses identify 139 loci associated with macular thickness in the UK Biobank cohort. *Hum Mol Genet* **28**, 1162–1172 (2019).

19. Sergouniotis, P. I. *et al.* Autoencoder-based phenotyping of ophthalmic images highlights genetic loci influencing retinal morphology and provides informative biomarkers. *Bioinformatics* **41**, (2024).

20. Jackson, V. E. *et al.* Multi-omic spatial effects on high-resolution AI-derived retinal thickness. *Nat Commun* **16**, 1317 (2025).

21. Maryam Zekavat, S. *et al.* Phenome-and genome-wide analyses of retinal optical coherence tomography images identify links between ocular and systemic health. *Sci. Transl. Med* **16**, 4517 (2024).

22. Rajesh, A. E. *et al.* Machine learning derived retinal pigment score from ophthalmic imaging shows ethnicity is not biology. *Nature Communications* **16**, (2025).

23. Mbatchou, J. *et al.* Computationally efficient whole-genome regression for quantitative and binary traits. *Nat Genet* **53**, 1097–1103 (2021).

24. Yang, J. *et al.* Conditional and joint multiple-SNP analysis of GWAS summary statistics identifies additional variants influencing complex traits. *Nat Genet* **44**, 369–375 (2012).

25. Bulik-Sullivan, B. *et al.* LD score regression distinguishes confounding from polygenicity in genome-wide association studies. *Nat Genet* **47**, 291–295 (2015).

26. Buniello, A. *et al.* Open Targets Platform: facilitating therapeutic hypotheses building in drug discovery. *Nucleic Acids Res* **53**, D1467–D1475 (2025).

27. Appukuttan, B., Giridhar, A., Gopalakrishnan, M. & Sivaprasad, S. Normative spectral domain optical coherence tomography data on macular and retinal nerve fiber layer thickness in Indians. *Indian J Ophthalmol* **62**, 316–321 (2014).

28. Wu, J. *et al.* Clinical science Macular thickness and its associated factors in a Chinese rural adult population: the Handan Eye Study. *Br J Ophthalmol* **107**, 1864–1872 (2023).

29. *Using Population Descriptors in Genetics and Genomics Research*. (National Academies Press, Washington, D.C., 2023). doi:10.17226/26902.

30. Babaker, R. *et al.* Risk factors for age-related macular degeneration: Updated systematic review and meta-analysis. *Medicine (United States)* **104**, e41599 (2025).

31. Maugeri, A., Barchitta, M. & Agodi, A. The association between complement factor H rs1061170 polymorphism and age-related macular degeneration: a comprehensive meta-analysis stratified by stage of disease and ethnicity. *Acta Ophthalmol* **97**, e8–e21 (2019).

32. Ross, R. J. *et al.* The LOC387715 Polymorphism and Age-Related Macular Degeneration: Replication in Three Case-Control Samples. *Invest Ophthalmol Vis Sci* **48**, 1128–1132 (2007).

33. Shahid, H. *et al.* Age-related macular degeneration: the importance of family history as a risk factor. *British Journal of Ophthalmology* **96**, 427–431 (2012).

34. Curcio, C. A., Kar, D., Owsley, C., Sloan, K. R. & Ach, T. Age-Related Macular Degeneration, a Mathematically Tractable Disease. *Invest Ophthalmol Vis Sci* **65**, (2024).

35. Lejoyeux, R. *et al.* Genetic analysis of participants with foveal hypoplasia. *Ophthalmic Genet* 1–4 (2025) doi:10.1080/13816810.2025.2520411.

36. Bakker, R. *et al.* The retinal pigmentation pathway in human albinism: Not so black and white. *Prog Retin Eye Res* **91**, (2022).

37. Ayala, G. D. *et al.* Assessing foveal structure in individuals with TYR R402Q and S192Y hypomorphic alleles. *Ophthalmology Science* **1**, 100077 (2021).

38. Jones, W. D. *et al.* De novo mutations in MLL cause Wiedemann-Steiner syndrome. *Am J Hum Genet* **91**, 358–364 (2012).

39. Choi, J., Joisher, H. N. V., Gill, H. K., Lin, L. & Cepko, C. Characterization of the development of the high-acuity area of the chick retina. *Dev Biol* **511**, 39–52 (2024).

40. da Silva, S. & Cepko, C. L. Fgf8 expression and degradation of retinoic acid are required for patterning a high-acuity area in the retina. *Dev Cell* **42**, 68-81.e6 (2017).

41. Ogino, J. & Dou, Y. Histone methyltransferase KMT2A: Developmental regulation to oncogenic transformation. *J Biol Chem* **300**, 107791 (2024).

42. Sun, C., Zhang, X., Ruzycki, P. A. & Chen, S. Essential Functions of MLL1 and MLL2 in Retinal Development and Cone Cell Maintenance. *Front Cell Dev Biol* **10**, 829536 (2022).

43. Taneera, J. *et al.* Unraveling the significance of PPP1R1A gene in pancreatic β-cell function: A study in INS-1 cells and human pancreatic islets. *Life Sci* **345**, (2024).

44. Keane, P. A. *et al.* Optical coherence tomography in the UK Biobank study - Rapid automated analysis of retinal thickness for large population-based studies. *PLoS One* **11**, (2016).

45. Xie, Y. *et al.* FGF/FGFR signaling in health and disease. *Signal Transduct Target Ther* **5**, (2020).

46. Xu, X. *et al.* Fibroblast growth factor receptor 2 (FGFR2)-mediated reciprocal regulation loop between FGF8 and FGF10 is essential for limb induction. *Development* **125**, 753–765 (1998).

47. Ding, W. *et al.* Sprouty2 downregulation plays a pivotal role in mediating crosstalk between TGF-β1 signaling and EGF as well as FGF receptor tyrosine kinase-ERK pathways in mesenchymal cells. *J Cell Physiol* **212**, 796–806 (2007).

48. Kuracha, M. R. *et al.* Spry1 and Spry2 are necessary for lens vesicle separation and corneal differentiation. *Invest Ophthalmol Vis Sci* **52**, 6887–6897 (2011).

49. Tomita, H. *et al.* The Protein Tyrosine Phosphatase Receptor Delta Regulates Developmental Neurogenesis. *Cell Rep* **30**, 215-228.e5 (2020).

50. Badde, A., Bumsted-O'Brien, K. M. & Schulte, D. Chick receptor protein tyrosine phosphatase λ/ψ (cRPTPλ/cRPTPψ) is dynamically expressed at the midbrain-hindbrain boundary and in the embryonic neural retina. *Gene Expression Patterns* **5**, 786–791 (2005).

51. Sampson, D. M., Dubis, A. M., Chen, F. K., Zawadzki, R. J. & Sampson, D. D. Towards standardizing retinal optical coherence tomography angiography: a review. *Light Sci Appl* **11**, 63 (2022).

52. Dubis, A. M. *et al.* Relationship between the foveal avascular zone and foveal pit morphology. *Invest Ophthalmol Vis Sci* **53**, 1628–1636 (2012).

53. Kreis, J. & Carroll, J. Applications of Adaptive Optics Imaging for Studying Conditions Affecting the Fovea. *Annu Rev Vis Sci* **35**, 239–262 (2024).

54. Yan, Q. *et al.* Deep-learning-based prediction of late age-related macular degeneration progression. *Nat Mach Intell* **2**, 141–150 (2020).

55. Warwick, A. N. *et al.* UK Biobank retinal imaging grading: methodology, baseline characteristics and findings for common ocular diseases. *Eye (Basingstoke)* **37**, 2109–2116 (2023).

56. Munafò, M. R., Tilling, K., Taylor, A. E., Evans, D. M. & Smith, G. D. Collider scope: When selection bias can substantially influence observed associations. *Int J Epidemiol* **47**, 226–235 (2018).

57. Schoeler, T. *et al.* Participation bias in the UK Biobank distorts genetic associations and downstream analyses. *Nat Hum Behav* **7**, 1216–1227 (2023).

58. Patel, P. J. *et al.* Spectral-domain optical coherence tomography imaging in 67 321 adults: Associations with macular thickness in the UK biobank study. *Ophthalmology* **123**, 829–840 (2016).

59. Julian, T., Fitzgerald, T., Birney, E. & Sergouniotis, P. I. Pigmentation and retinal pigment epithelium thickness: a study of the phenotypic and genotypic relationships between ocular and extraocular pigmented tissues. Preprint at https://doi.org/10.1101/2024.12.04.626809 (2024).

60. Zhou, Y. *et al.* AutoMorph: automated retinal vascular morphology quantification via a deep learning pipeline. *Transl Vis Sci Technol* **11**, (2022).

61. Romero-Bascones, D. *et al.* Foveal pit morphology characterization: A quantitative analysis of the key methodological steps. *Entropy* **23**, (2021).

62. Constantinescu, A. E. *et al.* A framework for research into continental ancestry groups of the UK Biobank. *Hum Genomics* **16**, (2022).

63. Auton, A. *et al.* A global reference for human genetic variation. *Nature* vol. 526 68–74 Preprint at https://doi.org/10.1038/nature15393 (2015).

64. Purcell, S. *et al.* PLINK: A tool set for whole-genome association and population-based linkage analyses. *Am J Hum Genet* **81**, 559–575 (2007).

65. Alexander, D. H., Novembre, J. & Lange, K. Fast model-based estimation of ancestry in unrelated individuals. *Genome Res* **19**, 1655–1664 (2009).

66. Cunningham, F. *et al.* Ensembl 2022. *Nucleic Acids Res* **50**, D988–D995 (2022).

67. Ochoa, D. *et al.* Open Targets Platform: Supporting systematic drug-target identification and prioritisation. *Nucleic Acids Res* **49**, D1302–D1310 (2021).

68. Sollis, E. *et al.* The NHGRI-EBI GWAS Catalog: knowledgebase and deposition resource. *Nucleic Acids Res* **51**, D977–D985 (2023).

69. Myers, T. A., Chanock, S. J. & Machiela, M. J. LDlinkR: An R Package for Rapidly Calculating Linkage Disequilibrium Statistics in Diverse Populations. *Front Genet* **11**, (2020).

70. Bulik-Sullivan, B. *et al.* LD score regression distinguishes confounding from polygenicity in genome-wide association studies. *Nat Genet* **47**, 291–295 (2015).

71. Davidson-Pilon, C. lifelines: survival analysis in Python. *J Open Source Softw* **4**, 1317 (2019).

72. Seabold, S. & Perktold, J. Statsmodels: Econometric and Statistical Modeling with Python. *Proceeding of the 9th Python in Science Conference* http://statsmodels.sourceforge.net/ (2010).

73. Burgess, S., Butterworth, A. & Thompson, S. G. Mendelian randomization analysis with multiple genetic variants using summarized data. *Genet Epidemiol* **37**, 658–665 (2013).

74. Hemani, G. *et al.* The MR-Base platform supports systematic causal inference across the human phenome. *Elife* **7**, (2018).

75. Bowden, J. *et al.* Improving the visualization, interpretation and analysis of two-sample summary data Mendelian randomization via the Radial plot and Radial regression. *Int J Epidemiol* **47**, 1264–1278 (2018).

76. Burgess, S. & Thompson, S. G. Interpreting findings from Mendelian randomization using the MR-Egger method. *Eur J Epidemiol* **32**, 377–389 (2017).

77. Burgess, S. *et al.* Guidelines for performing Mendelian randomization investigations. *Wellcome Open Res* **4**, 186 (2019).

78. Bowden, J., Davey Smith, G., Haycock, P. C. & Burgess, S. Consistent Estimation in Mendelian Randomization with Some Invalid Instruments Using a Weighted Median Estimator. *Genet Epidemiol* **40**, 304 (2016).

79. Hartwig, F. P., Smith, G. D. & Bowden, J. Robust inference in summary data Mendelian randomization via the zero modal pleiotropy assumption. *Int J Epidemiol* **46**, 1985 (2017).

ACKNOWLEDGEMENTS

We acknowledge the following sources of funding: the Wellcome Trust (224643/Z/21/Z, Clinical Research Career Development Fellowship to P.I.S.); the UK National Institute for Health Research (NIHR) Clinical Lecturer Programme (CL-2017-06-001 to P.I.S.); the NIHR Manchester Biomedical Research Centre (NIHR 203308 to P.I.S. and G.C.B.); the EMBL European Bioinformatics Institute (EMBL-EBI) (S.T., T.F. and E.B.); Medical Research Council (MRC) Clinical Research Training Fellowship (MR/Z504105/1, to T.H.J), and the Howard Hughes Medical Institute (C.L.C). Research reported in this publication was supported in part by the National Eye Institute of the National Institutes of Health (NIH) under award numbers R01EY017607 and R01EY033580. The content is solely the responsibility of the authors and does not necessarily represent the official views of the NIH.

The UK Biobank Eye and Vision Consortium is supported by funding from the NIHR Biomedical Research Centre at Moorfields Eye Hospital and UCL Institute of Ophthalmology, the Alcon Foundation and the Desmond Foundation. The

complete list of members of this Consortium can be found in the Supplementary Information.

AUTHOR CONTRIBUTIONS STATEMENT

P.I.S, D.J.G and T.H.J conceived and designed the experiments. The UK Biobank Eye and Vision Consortium, D.R, H.N.V.J, U.A, M.B, T.F, E.B, C.L.C, J.C and P.I.S provided datasets and analytical tools. D.J.G, D.R, T.H.J, S.T, H.N.V.J, T.F, C.L.C, and P.I.S analyzed the data. D.J.G wrote the manuscript with support from P.I.S and T.H.J. All authors critically revised and approved the manuscript. P.I.S, D.J.G and T.H.J conceived and designed the experiments. The UK Biobank Eye and Vision Consortium, D.R, H.N.V.J, U.A, M.B, T.F, E.B, C.L.C, J.C and P.I.S provided datasets and analytical tools. D.J.G, D.R, T.H.J, S.T, H.N.V.J, T.F, C.L.C, and P.I.S analyzed the data. D.J.G wrote the manuscript with support from P.I.S and T.H.J. All authors critically revised and approved the manuscript.

COMPETING INTERESTS STATEMENT

E.B. is a paid consultant and equity holder of Oxford Nanopore, a paid consultant to Dovetail, and a non-executive director of Genomics England, a limited company wholly owned by the UK Department of Health and Social Care. All other authors declare no competing interests. D.R. is an employee of RetinAI, but performed this work independently of RetinAI.

UK Biobank Eye and Vision Consortium

Jay E. Self,[9,10] Graeme C. Black[1,11], Panagiotis I. Sergouniotis[1,3,5,11]

[1] Division of Evolution, Infection and Genomics, School of Biological Sciences, Faculty of Biology, Medicine and Health, University of Manchester, Manchester, UK.

[3] Manchester Royal Eye Hospital, Manchester University NHS Foundation Trust, Manchester, UK.

[5] European Molecular Biology Laboratory, European Bioinformatics Institute (EMBL-EBI), Wellcome Genome Campus, Cambridge, UK

[9] Clinical and Experimental Sciences, Faculty of Medicine, University of Southampton, Southampton, UK

[10] Southampton Eye Unit, University Hospital Southampton NHS Foundation Trust, Southampton, UK

[11] Manchester Centre for Genomic Medicine, Saint Mary's Hospital, Manchester University NHS Foundation Trust, Manchester, UK

A full list of members appears in the Supplementary Information.